Journal of Materials Science & Technology 270 (2026) 36–48

Contents lists available at ScienceDirect

Journal of Materials Science & Technology

journal homepage: www.elsevier.com/locate/jmst

Research Article

Revealing the complex chemistry of grain boundaries in K-doped $BaFe_2As_2$ with atom probe tomography

Laura Lain Rodriguez[a,*], Benjamin M. Jenkins[a], Shah Alam Limon[b,c], Chiara Tarantini[b], Eric Hellstrom[b,c,d], Fumitake Kametani[b,d], Michael P. Moody[a], Chris R.M. Grovenor[a], Susie Speller[a]

[a] Department of Materials, University of Oxford, Parks Road, Oxford OX1 3PH, UK
[b] Applied Superconductivity Center, National High Magnetic Field Laboratory, Florida State University, 2031 E. Paul Dirac Dr., Tallahassee, FL, USA
[c] Materials Science and Engineering, FAMU-FSU College of Engineering, Florida State University, 2525 Pottsdamer St., Tallahassee, FL, USA
[d] Mechanical and Aerospace Engineering, FAMU-FSU College of Engineering, Florida State University, 2525 Pottsdamer St., Tallahassee, FL, USA

ARTICLE INFO

Article history:
Received 29 September 2025
Revised 6 January 2026
Accepted 8 January 2026
Available online 22 January 2026

Keywords:
Iron-based superconductors
K-Doped Ba-122
Critical current density
Granular superconductors
Atom probe tomography
Gibbsian interfacial excess

ABSTRACT

Iron-based superconductors have attractive properties for high-field applications, but there is a lack of understanding of the effect of grain boundary chemistry on the in-field performance. The near atomic-scale resolution, ppm sensitivity and 3D analysis offered by atom probe tomography make it a powerful tool to investigate the nanoscale structure and chemistry of these defects in fine-grained K-doped $BaFe_2As_2$ samples. A computational method to systematically extract and compare the Gibbsian interfacial excess of chemical species across grain boundaries has been explored in this work. The robustness of the method has been tested by evaluating the effects of selected variables on simulated APT datasets. The accuracy and precision of the calculated Gibbsian interfacial excess were found to be stable over a range of analysis conditions: varying grain boundary widths and detection efficiencies, spatial precisions below 1.5 nm, and bin widths between 1.2 and 1.6 nm. For the K-doped $BaFe_2As_2$ samples studied, segregation of As, Ba, K and impurities of O, Na, and Sb were found at grain boundaries. The Gibbsian excess values were found to vary widely between different boundaries, showing the complexity of the grain boundary chemistry in this material. Possible links between the observed critical current density (J_c) of these samples and their nano- and micro-structure have also been investigated and discussed.

1. Introduction

Since their discovery in 1911 [1], superconductors have led to numerous technological innovations, including Magnetic Resonance Imaging (MRI), magnets for particle accelerators, nuclear fusion reactors, and single photon detectors. Many of these applications rely on the large electrical current densities that can be passed through these materials without any resistance, but there is a limit to the key parameter, the critical current density (J_c), which is determined not only by the intrinsic properties of the superconductor but also by its microstructure. Maximising J_c by microstructural engineering has become a key focus for the development of materials for higher magnetic field applications, such as nuclear fusion, where the superconductor in reactor magnets is expected to operate at fields well above 10 T and carrying current densities over 10^5 A cm^{-2} [2].

The family of iron-based superconductors (IBSCs) emerged in 2008 [3,4], and is currently being explored as a candidate for these high field applications owing to their very high upper critical fields ($>$ 40 T) and J_c values exceeding 10^6 A cm^{-2} at 9 T in single crystals [5]. Compared to rare-earth cuprate superconductors (REBCO), which currently offer the highest J_c values in high fields [6,7], IBSCs have the advantages of being less anisotropic [8] and having a weaker J_c degradation with grain boundary misorientation angle [9], which could facilitate their adoption as more cost-effective and practical polycrystalline wires. Of the iron-based superconductors, the $BaFe_2As_2$ (or Ba-122) family has shown the highest J_c values in polycrystalline materials [10–12]. A variety of dopants have been studied for Ba-122 materials, with K commonly partly substituting for Ba, as this results in both increasing the critical temperature (T_c) up to 38 K and a wider superconducting phase region [12], making it easier to define reliable synthesis conditions.

---

* Corresponding author.
E-mail address: laura.lainrodriguez@materials.ox.ac.uk (L. Lain Rodriguez).

https://doi.org/10.1016/j.jmst.2026.01.024

Although recent efforts by Han et al. have resulted in polycrystalline Ba-122 wires with a J_c of 4.5 × 10^5 A cm^{-2} at 4.2 K and 10 T [13] (above the practical target of 10^5 A cm^{-2} at 10 T), these are still outperformed by single crystals or highly textured samples. Previous studies on polycrystalline Ba-122 show that it is difficult to achieve high densities [14,15], and there is a tendency for chemical segregation and impurities at grain boundaries [14,16]. These factors can cause grain boundaries to become weak-links when the zone of reduced order parameter becomes wider than the coherence length of Ba-122 (1.2–2.4 nm) [17], which lowers the J_c values [14,16,18,19]. Very extensive studies of the properties of grain boundaries in REBCO have shown that a reduction in the local order parameter can be measured even in chemically clean (unsegregated) grain boundaries with misorientation angles greater than 5° [20], perhaps associated with loss of some oxygen [21,22], and that segregation of impurities will further damage the local superconducting properties [23]. The extent to which J_c in IBSC samples is limited by either the intrinsic properties of grain boundaries (arising directly from the misorientation of the crystal lattice) or extrinsic factors from processing, like impurity or dopant segregation, has not yet been properly resolved.

To gain a better understanding of the role grain boundaries play in Ba-122 superconductors, high-resolution characterisation of the grain boundary chemistry is required. This is complicated by the fact that these materials are often processed to give grain sizes below 500 nm because of the valuable contribution that grain boundaries have on the flux pinning properties [19]. There have been multiple studies using transmission electron microscopy (TEM) [14,16,18,19,24,25] where FeAs layers, oxide phases, and K segregation were found at grain boundaries. Additionally, these studies show that using high-purity precursors [14,16], processing the material in low oxygen and moisture environments [14,16], having an excess of K starting material [14], and using lower heat treatment temperatures of 600 °C [18] can all prevent the formation of impurities and secondary phases at grain boundaries, leading to improvements in J_c. However, quantifying chemical variations across boundaries remains challenging by TEM, especially when the orientation of a boundary with respect to the analysis direction is hard to control. Atom probe tomography (APT) offers near atomic-scale resolution, ppm sensitivity to all elements, and the capability to study complex materials in 3D [26], making it a very suitable tool to investigate grain boundaries and the nanoscale structure of IBSCs, but so far has only been applied sparingly to study them [27–29].

Grain boundary segregation in APT is often quantified by the Gibbsian interfacial excess, a thermodynamic measure of how many excess solute atoms per unit area there are at an interface compared to the average matrix concentration of solute [30,31]. This work firstly explores the validity of a new systematic Poisson-based method applicable to a variety of systems that identifies and calculates Gibbsian excess across grain boundaries analysed by APT, using simulated datasets. This automated method also presents advantages over currently implemented methods, leading to more reproducible results between users [32]. Secondly, this work quantifies the Gibbsian excess in grain boundaries of real K-doped $BaFe_2As_2$ bulks using the Poisson-based method described, with the goal of investigating if variations in J_c performance can be explained by the measured grain boundary chemistry in IBSC materials.

2. Experimental section

2.1. Synthesis

Three bulk samples of polycrystalline $Ba_{0.61}K_{0.39}Fe_2As_2$ were fabricated by powder processing [33]. High-purity precursors of each element were first mixed inside an Ar glovebox and ball milled for three different lengths of time corresponding to ball milling energy densities of 65, 100, and 200 MJ kg^{-1} to form the Ba-122 phase. The ball milling energy densities were chosen based on previous work by Tokuta et al. [25], which showed that 80 MJ kg^{-1} yielded the highest J_c in Co-doped $BaFe_2As_2$, whereas lower energy (20 MJ kg^{-1}) and much higher energy processes (590 MJ kg^{-1}) resulted in an incomplete mechanochemical reaction or poorly connected grain aggregates, respectively. The ball-milled powders were packed and sealed into Nb sheaths, then heat-treated at 750 °C for 10 h. The sheaths were removed, and the samples underwent a second ball milling stage at 40 MJ kg^{-1}, followed by re-packing and sealing into Nb sheaths, and a second heat treatment at 600 °C under a pressure of 193 MPa. This was done to minimise any secondary phases caused by incomplete reaction when initially forming the Ba-122 phase, and to sinter the powders into homogeneous bulks [18]. No texture was introduced during processing, resulting in randomly oriented polycrystalline bulk materials. After this preparation procedure, the samples were kept inside a desiccator in an Ar glovebox to limit reactions with moisture and oxygen.

Table 1
Sample dimensions of the three $Ba_{0.61}K_{0.39}Fe_2As_2$ bulks used for calculations of critical current density. Dimensions a and b were perpendicular to the applied magnetic field, whilst c was parallel to it.

Sample's ball milling energy density (MJ kg^{-1})	a (mm)	b (mm)	c (mm)
65	1.00	3.00	1.00
100	1.00	2.65	1.00
200	0.42	2.40	1.54

2.2. APT experiments

Sharp APT needles of the three $Ba_{0.61}K_{0.39}Fe_2As_2$ bulks were made by the focused ion beam (FIB) milling method developed by Larson et al. [34,35], using a Zeiss Crossbeam 540 Analytical FIB-SEM microscope. Sections of approximately 20 µm × 4 µm × 3.5 µm in size were milled out of the bulk surfaces, welded using Pt onto Si posts and progressively thinned to achieve needles with an end diameter of 20–40 nm [34].

The prepared needles were transferred to a local electrode atom probe instrument (Cameca LEAP 5000 XR). Atom probe running conditions were: laser mode with an energy of 30 pJ, a sample temperature of 50 K, a target detection rate of 0.2 %, and because of the need to detect the field evaporation of heavy as-containing molecular ions, a varying pulse rate frequency was used to keep a constant mass spectrum range up to 340 Da.

2.3. Magnetometry

Magnetisation measurements on three $Ba_{0.61}K_{0.39}Fe_2As_2$ bulk samples of the same batches as the ones produced for APT measurements were carried out on an Oxford Instruments vibrating sample magnetometer (VSM) at 14 T maximum field and a temperature of 4.2 K. The critical current density was extracted using the extended Bean model [36,37] using Eq. (1):

$$J_c = \frac{2\Delta m}{Va\left(1 - \frac{a}{3b}\right)} \tag{1}$$

where Δm is the difference in moment (in A m^2), V is the sample volume (in m^3), and a and b (in m) are the sample dimensions perpendicular to the applied field, where $a < b$. The samples were rectangular with dimensions summarised in Table 1.

3. Simulations and calculations

In order to investigate the accuracy of using APT to measure the composition and Gibbsian interfacial excess associated with grain boundaries (GB), a series of simulations was performed. Simulations were conducted for a variety of independent variables, summarised in Table 2.

As shown schematically in Fig. 1, each individual simulated volume was created as follows:

(1) A 25 nm × 25 nm × 30 nm volume with a simple cubic lattice (lattice parameter = 0.2 nm) was generated. This simplified crystal structure was chosen to unambiguously define the location of grain boundaries in the simulations [38].

(2) A grain boundary of the desired width was inserted into this volume such that the volume was divided into three regions: grain 1, the grain boundary, and grain 2.

Table 2
Summary of the parameters that were swept when generating the simulated APT volumes.

Variable	Units	Range	Step size
Grain boundary width	Atomic planes	1–6	1
Detection efficiency (η)	–	0.4–1.0	0.1
Spatial precision in the Z direction (Z precision)	nm	0.0–2	0.5
Bin width	nm	0.8–2.4	0.4

(3) The atoms in each region were probabilistically assigned a mass-to-charge-state ratio (Da) based on the desired composition of the three regions. Five different cases were investigated for each simulated volume, with Table 3 showing the assigned compositions of the various phases. Elements

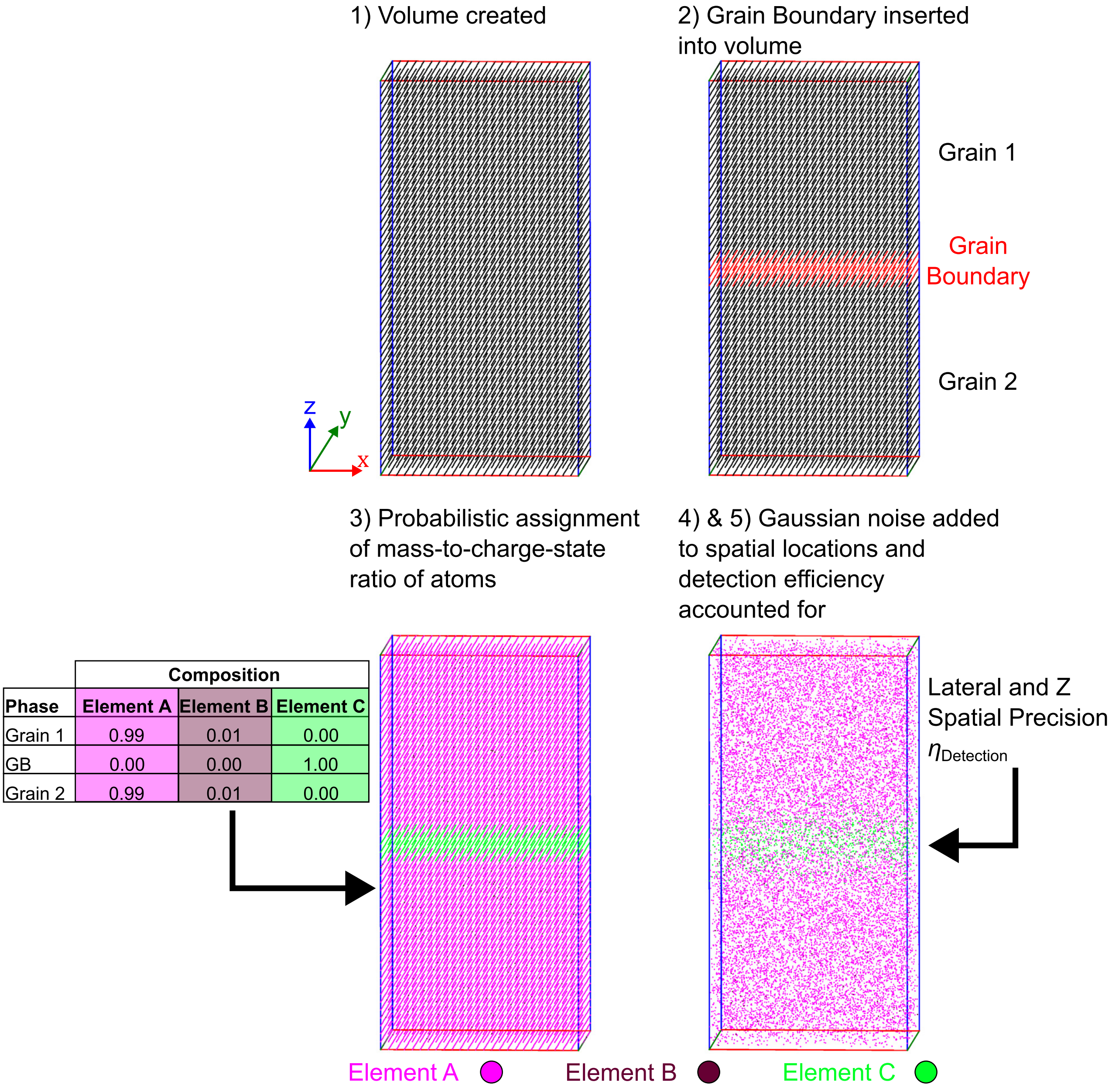

	Composition		
Phase	Element A	Element B	Element C
Grain 1	0.99	0.01	0.00
GB	0.00	0.00	1.00
Grain 2	0.99	0.01	0.00

Fig. 1. Schematic diagram showing steps (1)–(5) on how the simulated APT datasets were generated.

Table 3
Compositions of the different cases that were investigated for each simulated volume.

Case	Phase	Element A (Matrix)	Element B (Matrix)	Element C (Solute)	Physical scenario
1	Grain 1	1.00	0.00	0.00	Simplest case. Every atom at the GB is solute element C. No solute element C in the matrix.
	GB	0.00	0.00	1.00	
	Grain 2	1.00	0.00	0.00	
2	Grain 1	0.90	0.00	0.10	Some solute in the matrix. Every atom at the GB is of solute element C.
	GB	0.00	0.00	1.00	
	Grain 2	0.90	0.00	0.10	
3	Grain 1	0.90	0.00	0.10	More difficult case than case 2–solute in matrix and matrix atoms in GB.
	GB	0.20	0.00	0.80	
	Grain 2	0.90	0.00	0.10	
4	Grain 1	0.85	0.05	0.10	More difficult case than case 3–solute in matrix and matrix atoms in GB. Also third element (B) that does not segregate.
	GB	0.15	0.05	0.80	
	Grain 2	0.85	0.05	0.10	
5	Grain 1	0.70	0.00	0.30	Some solute in the matrix. Every atom at the GB is of solute element C. The composition of element C varies in grain 1 and grain 2.
	GB	0.00	0.00	1.00	
	Grain 2	0.90	0.00	0.10	
6	Grain 1	0.796	0.199	0.005	Smaller levels of segregation at the GB. More matrix atoms in GB. Representative of typical segregation seen in the $Ba_{0.61}K_{0.39}Fe_2As_2$ samples studied here.
	GB	0.784	0.196	0.02	
	Grain 2	0.796	0.199	0.005	

A and B were defined as forming the matrix material, and element C as the solute.

(4) Gaussian noise was added to the spatial location of the atoms based on the spatial precision (Z precision) for each simulation [39–41], to model the imperfect spatial resolution within an APT reconstruction [40,42–44]. The precision in the X–Y direction was also accounted for; however, since this was observed not to influence the Gibbs excess calculations, it is not discussed further here.
(5) Atoms were randomly extracted to account for the imperfect detection efficiency of current APT instruments [41,45].

The interfacial excess and the overall composition of each grain were then calculated for each unique simulation. This process was automated after user input of the following parameters: the α value used for statistical tests, the width of bins that the dataset is divided into (Bin Width), the name of the reference segregating element used for calculations (SE), and two distances that indicate the distance (x_1) beyond which the chemical composition of grain 1 is unaffected by the grain boundary and the distance (x_2) beyond which the chemical composition of grain 2 is unaffected by the grain boundary, respectively. The following process, shown schematically in Fig. 2, was then applied:

(1) The dataset was divided into bins of width ‘Bin Width’ in the direction perpendicular to the grain boundary.
(2) Two regions were extracted; the first including all distances within grain 1 up to x_1 and the second including all distances in grain 2 beyond x_2.
(3) The mean number of counts of the SE in each region was then measured. This distribution of counts of SE in the bins in each region was assumed to follow a Poisson distribution:

$$P(X=x)=\frac{e^{-\lambda}\times\lambda^{x}}{x!}, \tag{2}$$

where λ is the mean. The probability of observing the threshold number of counts of the SE that was statistically unlikely to occur in a bin (N_{SE}^{Th}) was then calculated for each sub volume using Eq. (3):

$$P\left[X\geq N_{SE}^{Th}\right]=1-\sum_{i=0}^{x-1}P\left(X=i\right)<\alpha_{Adjusted} \tag{3}$$

As multiple bins in the region of interest were tested, it was necessary to use the Šidák Correction [46] to adjust the significance level (α) and reduce the likelihood of making a Type II error (false negative):

$$\alpha_{Adjusted}=1-(1-\alpha)^{1/m} \tag{4}$$

where α is the original significance level, and m is the number of tests conducted (in this case, the number of bins in the region of interest).

(1) The position at which the grain boundary started ($x_{GB\ Start}$), was then calculated as the bin at which the number of counts of the SE first exceeded N_{SE}^{Th}. An equivalent process, based on the distribution of element SE in grain 2, was used to calculate where the grain boundary ended ($x_{GB\ End}$).
(2) The composition of the grain boundary region and its Gibbsian interfacial excess was then calculated using the equations proposed in [31]. The calculated grain boundary width was determined as the distance between $x_{GB\ Start}$ and $x_{GB\ End}$.

4. Results

4.1. Simulations

Fig. 3 shows how the calculated Gibbsian excess from the simulated datasets for composition cases 1–5 is affected by the independent variables investigated in this study (Table 2).

A representative subset of the results is shown in Fig. 3, where, unless explicitly plotted, the remaining variables were fixed to three grain boundary planes, a detection efficiency of 100 %, a Z precision of 0.5 nm and a bin width of 1.6 nm. Overall, the calculated Gibbsian excess values agreed closely with the expected ones and showed a weak dependence on the variables tested, except for data from simulation case 5, where the calculated Gibbsian excess was generally underestimated.

Fig. 4 shows the calculated Gibbsian excess data only for simulation case 6, which was chosen to more closely represent the real APT data from the $BaFe_2As_2$ samples studied here. Although in many cases the calculations agree with the built-in values, Fig. 4 also shows that spatial precisions worse than 1 nm, bin widths greater than 1.6 nm, and detection efficiencies below 70 % can all reduce the accuracy of the calculated Gibbsian excess, mostly resulting in underestimating the excess value of 1.125 atoms nm^{-2}. A bin width of 1.6 nm was found to provide a smaller variability in the resulting Gibbsian excess for the many spatial resolutions tested (see supplementary material). The initial set width

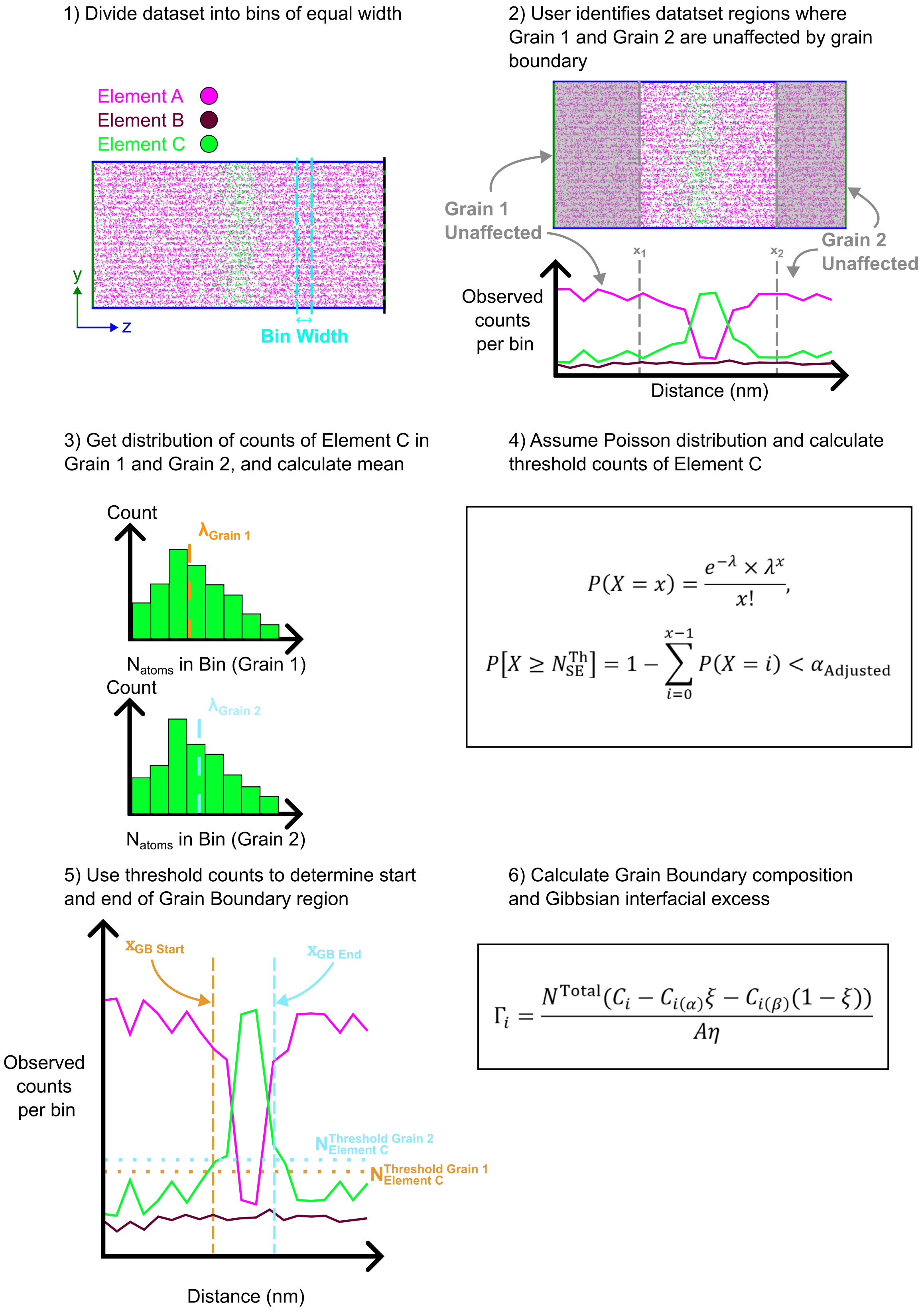
1) Divide dataset into bins of equal width

2) User identifies datatset regions where Grain 1 and Grain 2 are unaffected by grain boundary

3) Get distribution of counts of Element C in Grain 1 and Grain 2, and calculate mean

4) Assume Poisson distribution and calculate threshold counts of Element C

$$P(X = x) = \frac{e^{-\lambda} \times \lambda^{x}}{x!},$$

$$P\left[X \geq N_{\mathrm{SE}}^{\mathrm{Th}}\right] = 1 - \sum_{i=0}^{x-1} P(X = i) < \alpha_{\mathrm{Adjusted}}$$

5) Use threshold counts to determine start and end of Grain Boundary region

6) Calculate Grain Boundary composition and Gibbsian interfacial excess

$$\Gamma_i = \frac{N^{\mathrm{Total}}\left(C_i - C_{i(\alpha)}\xi - C_{i(\beta)}(1-\xi)\right)}{A\eta}$$

Fig. 2. Schematic diagram showing the use of the poisson method to determine the bounds of the grain boundary region. In this example, element C is the element that shows segregation to the boundary.

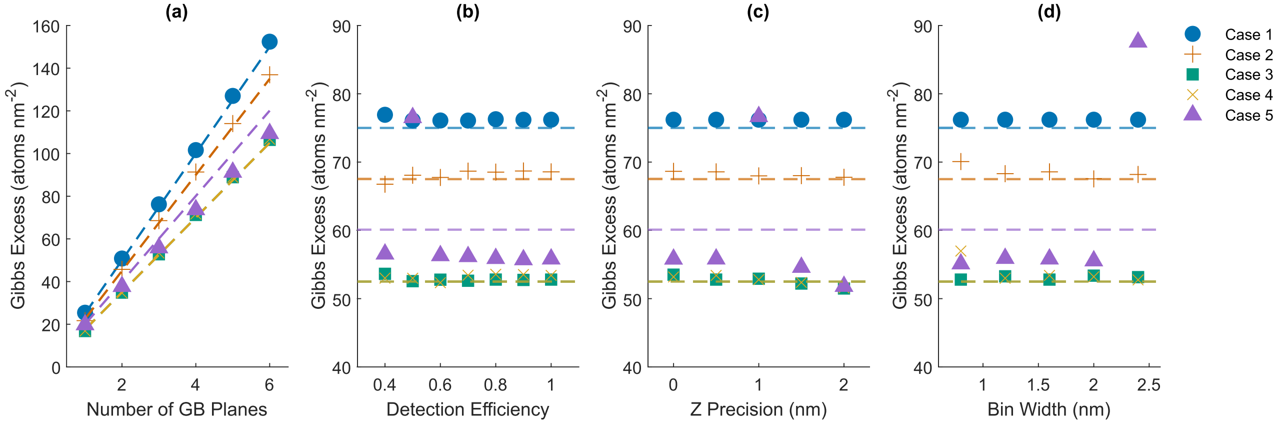

Fig. 3. Calculated Gibbsian excess of simulation cases 1–5 plotted against (a) the initial number of grain boundary planes, (b) detection efficiency, (c) precision in the Z-axis and (d) the bin width. Dashed lines represent the expected Gibbsian excess values for each case. When not constituting the *x*-axis of the individual subplots, variables were set to 3 grain boundary planes, 100 % detection efficiency, a Z precision of 0.5 nm and a bin width of 1.6 nm.

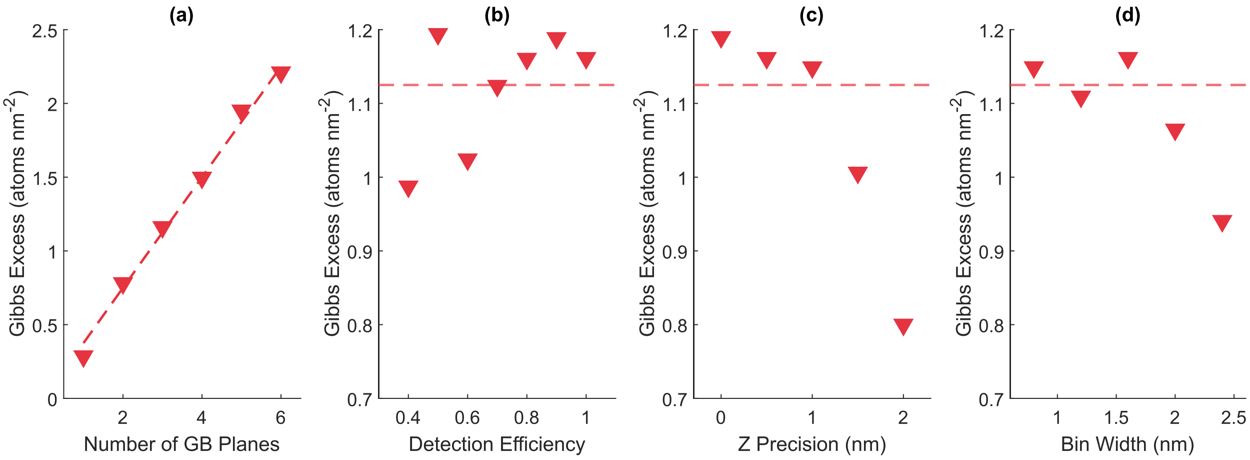

Fig. 4. Calculated Gibbsian excess of simulation case 6 plotted against (a) the initial number of grain boundary planes, (b) detection efficiency, (c) precision in the Z-axis and (d) the bin width. Dashed lines represent the expected Gibbsian excess values. When not constituting the x-axis of the individual subplots, variables were set to 3 grain boundary planes, 100 % detection efficiency, a Z precision of 0.5 nm and a bin width of 1.6 nm.

of the grain boundary did not detrimentally affect the accuracy of the results.

Comparing the different simulation cases, good agreement was found between the expected and calculated Gibbsian excess values, even for more complicated cases like 3 and 4, where there was a significant concentration of matrix element atoms at the grain boundary and solute atoms in the matrix. The exception to this was case 5, which is the only case with a difference in the compositions of the two grains, which generally resulted in an underestimation of the Gibbsian excess and incorrect assignment of the grain boundary start and end points.

4.2. Application to experimental APT data

This method to calculate Gibbsian interfacial excess was applied to two APT datasets from the 200 MJ kg^{-1} ball milling energy density $Ba_{0.61}K_{0.39}Fe_2As_2$ sample (Fig. 5). Owing to the small grain size of these samples (~60–150 nm), it was expected that typical APT volumes of approximately 400 nm in length and 20–100 nm in diameter would contain several grain boundaries. Fe_2O ions were found to be preferentially detected from boundaries, and were therefore used to locate seven grain boundaries contained in the volume analysed in these two datasets. The 3D interconnected geometry of these planar features suggests that they are grain boundaries, and that most boundaries contain some oxygen. There are several possible sources of this O impurity, including pre-existing oxidation on the bare surface of raw element materials from the supplier, or exposure of the Ba-122 powders to air and moisture after the 1st heat treatment [14,16,27]. Alternatively, the reacted bulks may have experienced degradation through exposure to atmospheric oxygen and moisture when transporting them between different locations and analysis instruments, with, for instance, approximately 10 min of exposure to air each time atom probe specimens were transferred from the FIB to the LEAP. In addition to O, impurities of Na (from the K source) and Sb (from the As starting powder) were also found segregated at grain boundaries. Cuboidal regions of interest (ROIs) were placed perpendicularly across the grain boundary planes, with a 25 nm × 25 nm cross section and 20 nm length. The Gibbsian excess of O (Fig. 5(c)) was evaluated by using concentration profiles with a bin width of 1.6 nm across these ROIs, and an α value of 0.05 to establish the thresholds at which the counts in a bin are considered statistically unlikely to occur within a grain.

Fig. 5(c) shows significant variation in the calculated Gibbsian excess of oxygen across these seven grain boundaries. The calculated excess depended on the choice of reference segregating el-

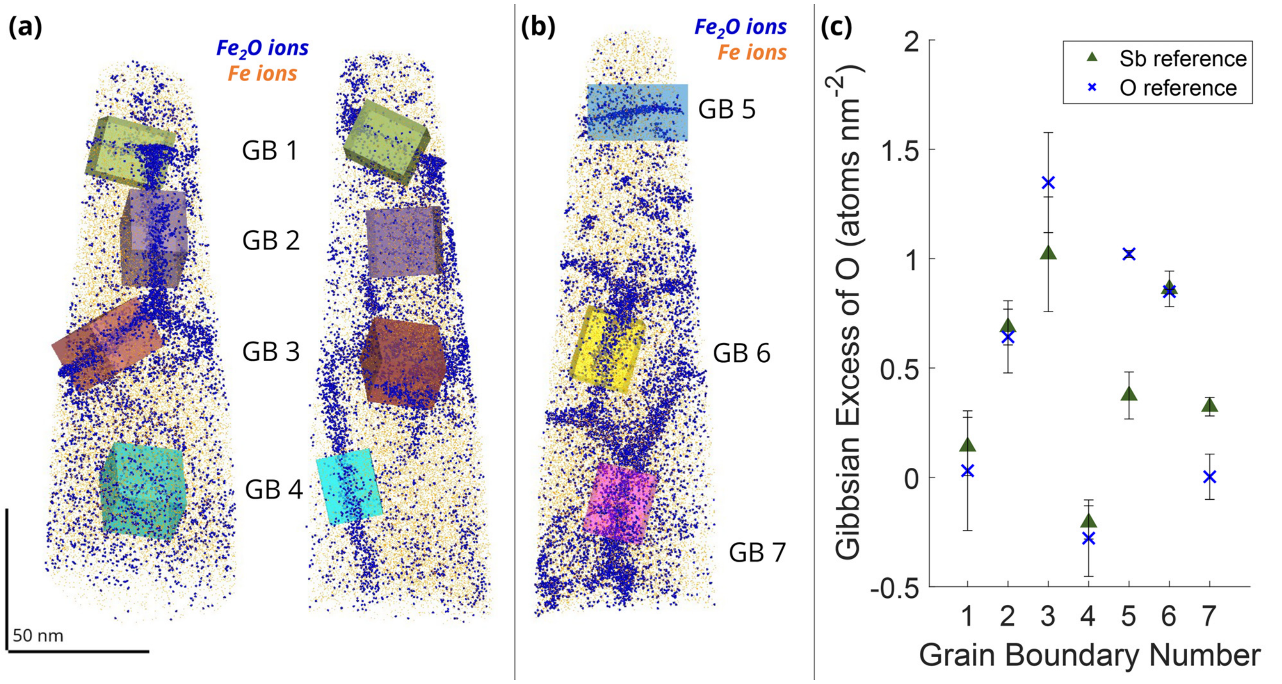

Fig. 5. Atom probe reconstructions from two separate datasets from the 200 MJ kg^{-1} sample, revealing grain boundaries highlighted by Fe$_2$O ions: (a) grain boundaries 1–4 at different rotations of the same dataset and (b) grain boundaries 5–7 in a different dataset. The cuboids shown are the regions of interest used to calculate Gibbsian interfacial excess. (c) Calculated Gibbsian interfacial excess for O from the grain boundaries in (a, b), using Sb and O as the reference segregating elements to establish the start and end points of grain boundaries. Error bars represent standard errors.

ement used to define the grain boundary limits (in this case, Sb or O), but in these cases, the relative changes in excess across the seven boundaries were mostly independent of the choice of reference element. Since the spatial precision along the analysis axis of an APT reconstruction is expected to be higher than that perpendicular to it [42,43], and as shown by the simulation results (Fig. 4(c)), the orientation of the grain boundaries to the tip axis might influence the calculated Gibbsian excess values. To explore this, Fig. 5(c) compares results from boundaries with different orientations with respect to the analysis axis. However, boundaries with similar alignment to the analysis axis showed notable variations in the calculated Gibbsian excess of oxygen (with GBs 1, 3, and 5 being more perpendicular and 2, 4, 6, and 7 more parallel to the tip axis). Hence, we conclude that the Gibbsian excess differences seen across the similarly oriented boundaries are likely to be real indications of variability in segregation behaviour to GBs in this superconductor. The bin width used in the calculations was also found to influence the resulting Gibbsian excess, but again, the relative differences in excess values remained comparable. A bin width of 1.6 nm was used for the Gibbsian excess comparisons between boundaries, as supported by the simulation results above, as well as providing effective smoothing of statistical counting noise in the segregation profiles.

Overall, 15 APT reconstructions from these $Ba_{0.61}K_{0.39}Fe_2As_2$ samples were studied, and Gibbsian interfacial excess values were extracted for 15 grain boundaries (Fig. 6). In addition to contamination with O, Na, and Sb impurities, careful analysis shows that the composition of the grain boundaries is often not uniform, with different boundaries showing different segregating elements. For example, in the dataset in Fig. 7(a), there is an increase in As, O, and Sb, and a depletion of Fe, Ba, and K at the boundary, whereas in Fig. 7(b) the boundary is depleted in Fe and As, but shows an increase in concentration of Ba, K, O, Na, and Sb. Varying levels of segregation of each element were also observed, even within samples made using the same synthesis conditions, and no clear correlation was found between synthesis conditions and the Gibbsian excess at grain boundaries (see Discussion). The segregation of matrix elements at the boundaries is linked in the literature to incomplete reaction of the starting powders to produce the ‘122’ phase [16], or from reaction with O segregated at boundaries (particularly seen for K and Ba in previous work [14]).

In addition to grain boundary segregation, APT has revealed other nanoscale inhomogeneities in the $Ba_{0.61}K_{0.39}Fe_2As_2$ samples. These are oxides of Ba and As, the FeAs secondary phase (Fig. 8) and significant porosity best shown during sample preparation (see supplementary material). It is worth noting that FeAs was not found to wet the grain boundaries in the APT datasets studied, but it has been seen at larger scales through EDX characterisation (see supplementary material), and could be a cause of poor connectivity in all samples. BaO impurities were found both at the nano-scale in the APT data and at the micron-scale by SEM-EDX.

Fig. 9 shows data from three $Ba_{0.61}K_{0.39}Fe_2As_2$ bulk samples of the same batch but not identical to those studied with the atom probe. Fig. 9(a) shows the calculated J_c at 4.2 K from the magnetisation curves of the three bulk samples. The calculated J_c was found to be highest overall for the 100 MJ kg^{-1} sample, indicating effective flux pinning and a better intergrain connectivity compared to the other two samples. Although the 65 MJ kg^{-1} sample showed a comparable J_c to that of the 200 MJ kg^{-1} sample at smaller applied fields, it showed less field dependence and a greater J_c at higher fields than the 200 MJ kg^{-1} sample. This indicates the 65 MJ kg^{-1} sample may have a poorer connectivity similar to that of the 200 MJ kg^{-1} sample, but with stronger flux pinning than the 200 MJ kg^{-1} sample. The ball milling energy density was also related to the grain size obtained from TEM imaging, and to the FeAs phase fraction from XRD Rietveld analysis, shown in Fig. 9(b, c), respectively. We note no significant correlation between the J_c values of the three samples and the calculated Gibbsian excesses at the grain boundaries studied, although significant concentrations of O were found in almost every grain boundary.

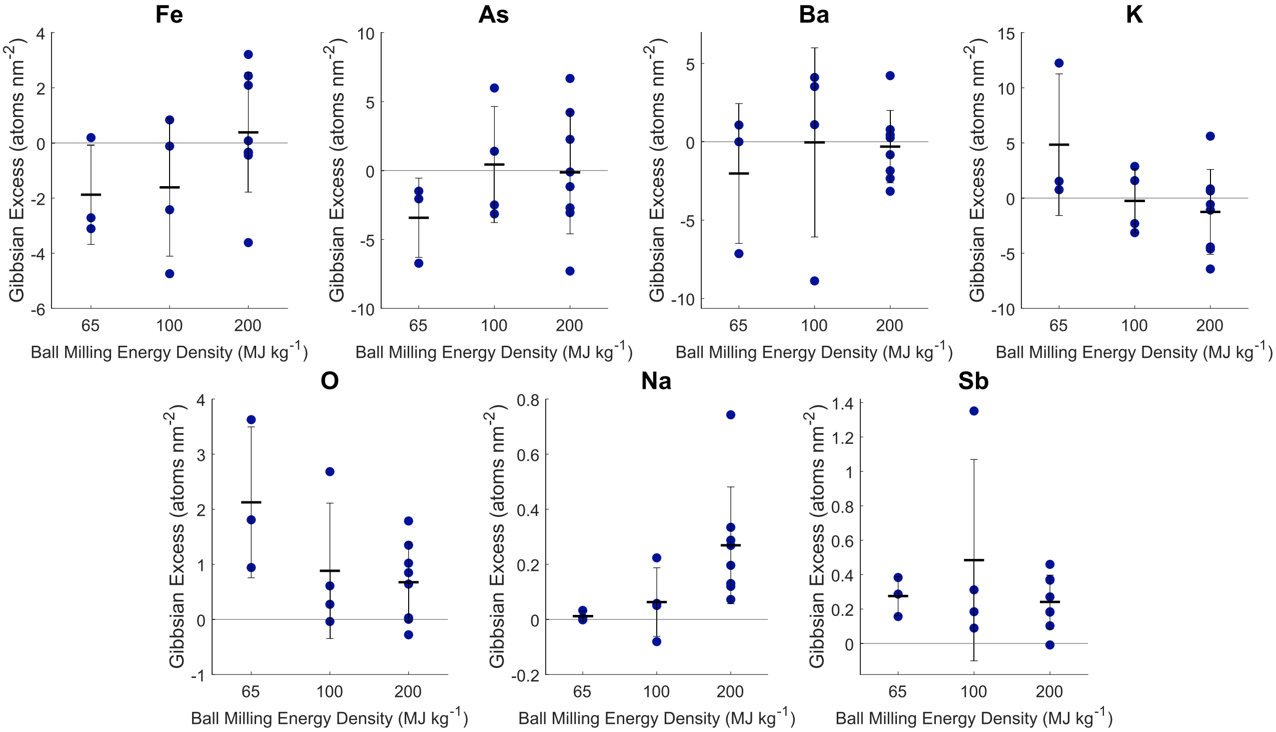

Fig. 6. Calculated Gibbsian interfacial excess values for three $Ba_{0.61}K_{0.39}Fe_2As_2$ samples manufactured with different ball milling energies, using O atoms as the reference to identify grain boundary regions. Horizontal black dashes represent averages, and error bars denote standard errors.

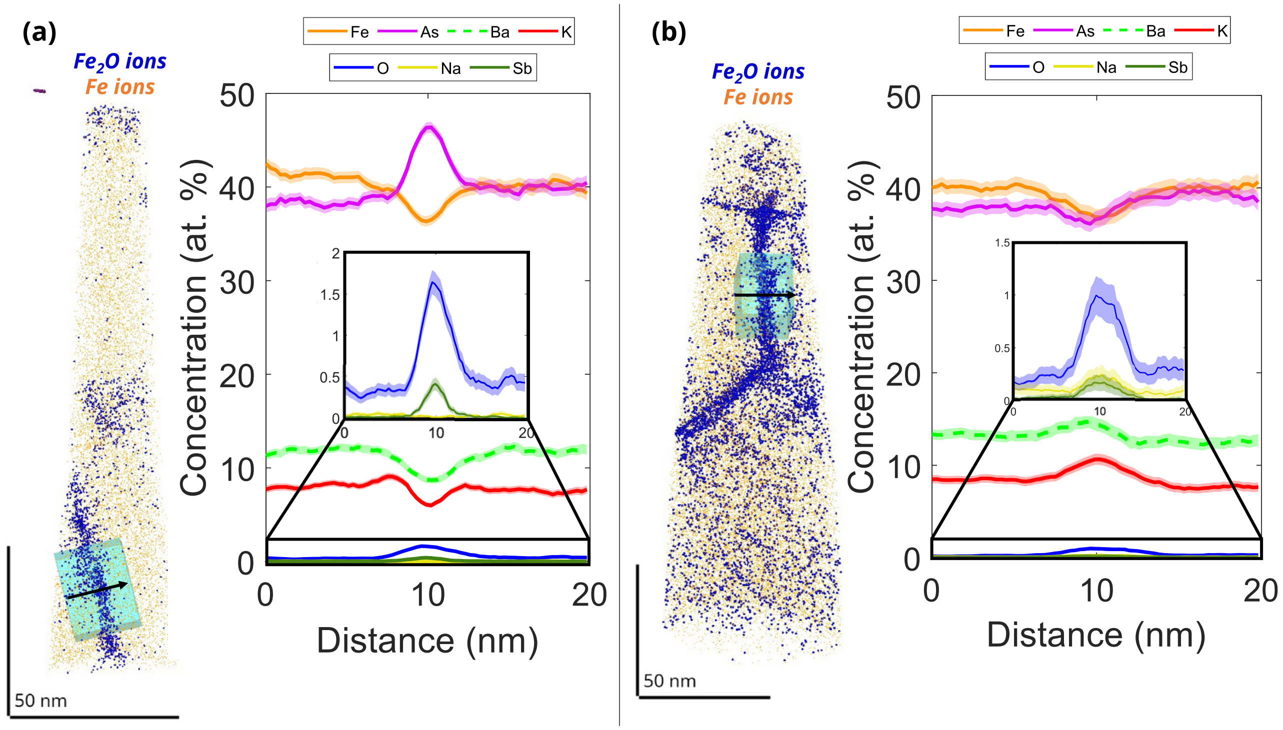

Fig. 7. Two atom probe datasets and their corresponding 1D concentration profiles across cuboidal regions of interest placed across individual grain boundaries. The dataset in (a) was extracted from the 100 MJ kg^{-1} sample, and the dataset in (b) is from the 200 MJ kg^{-1} sample.

5. Discussion

5.1. Validity of the Gibbsian excess method

We have shown that the computational method discussed in this study to extract Gibbsian interfacial excess could be a useful tool for more detailed studies of grain boundary chemistry in IBSC materials. Firstly, it provides a systematic way to define grain boundary limits, and removing user uncertainty from manually defining these bounds can improve the validity of any comparisons drawn between data from different samples. Except for the results from case 5, where the compositions of the 2 surround-

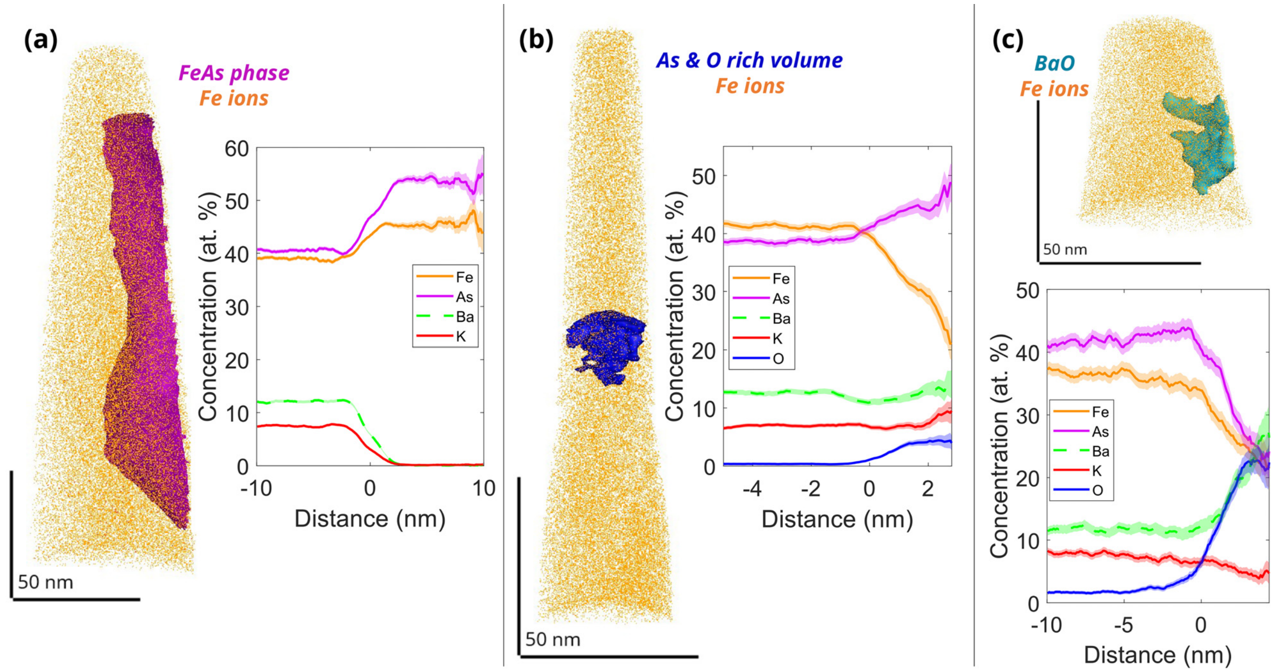

Fig. 8. Examples of nanoscale inhomogeneities found in APT datasets from the $Ba_{0.61}K_{0.39}Fe_2As_2$ samples and corresponding plots of concentration against radial distance from the surface of the inhomogeneities, for (a) the FeAs phase in the 200 MJ kg^{-1} sample, (b) As and O segregation in the 100 kg^{-1} sample, and (c) BaO in the 65 MJ kg^{-1} sample.

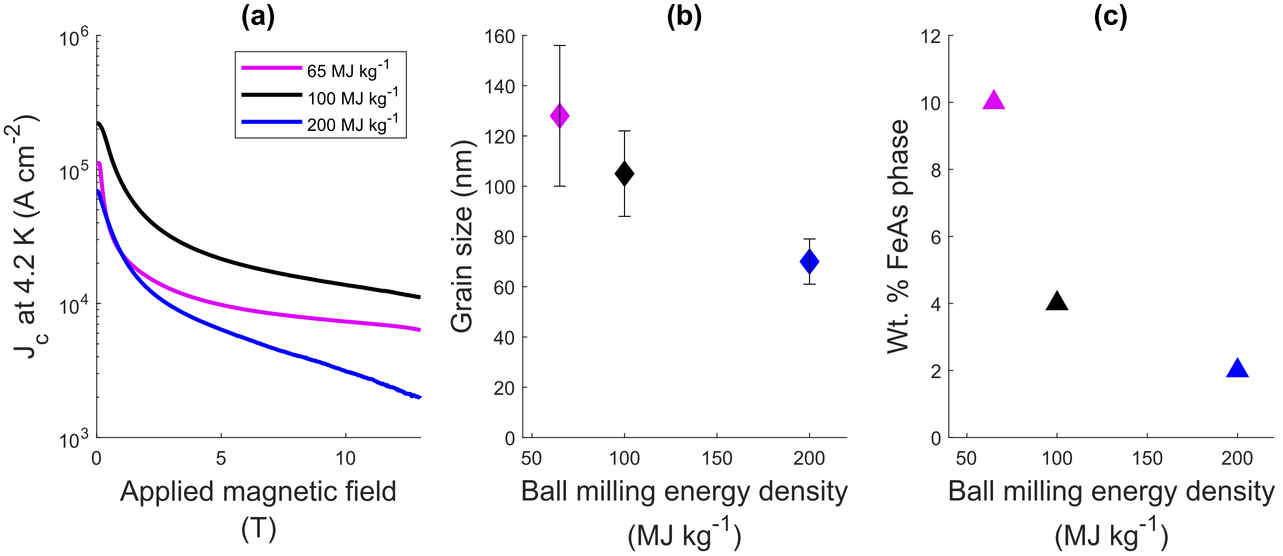

Fig. 9. Relationship between the ball milling energy density used during synthesis of the three $Ba_{0.61}K_{0.39}Fe_2As_2$ bulks and (a) the calculated critical current density J_c at field measured at 4.2 K [33], (b) grain size from TEM data [33], and (c) FeAs phase fraction from XRD measurements [47].

ing grains were allowed to vary, the simulations generally showed good agreement between the expected and calculated Gibbsian excess. The accuracy of the calculated excess values was not significantly affected by the detection efficiency, initial grain boundary width or bin width, and was not significantly reduced by low spatial resolution. The utility of the extracted excess values is further supported by the comparisons of real grain boundaries in $Ba_{0.61}K_{0.39}Fe_2As_2$ in Fig. 5(c), showing that segregation differences found through this method are not the result of changes in spatial resolution inherent in APT analysis. The observed Gibbsian excess variations suggest there is a very complex segregation landscape in these materials, not simply described by an excess or deficiency of any one element or impurity.

On the other hand, there are some important limitations to the method that must be considered. Firstly, the simulations showed that low spatial precisions (> 1 nm) and large bin widths (2–2.4 nm) can result in less accurate determinations of excess values. This is likely because both factors can cause blurring of the solute segregation profile within the APT reconstruction at the grain boundary edges, which can result in incorrectly defined bounds of the interface and, in turn, an erroneous extraction of Gibbsian excess. Typical quoted spatial resolutions in APT range from near-atomic to 1.1 nm [26,40], but they are highly dependent on the analysis conditions (temperature, laser or voltage mode) [40], the direction within an APT dataset [42,43], and the material being studied [44]. However, too small a bin width can also lead to erroneous data, with Tegg et al. showing it can lead to higher compositional uncertainties [48]. In some simulations of case 5 with a bin width of 0.8 nm (see supplementary material), due to higher levels of noise, bins in the matrix with solute counts higher than the established threshold were incorrectly selected as the bounds of the interface. This led to artificially wide grain boundaries with large negative Gibbsian excess values. In the case of APT datasets, a 1.6 nm bin width was found to give a balance between smoothing noise in the counts whilst minimising blurring of the interfacial segregation into the grains. The calculated Gibbsian excess using this bin width was also influenced to a lesser extent by the different spatial precisions tested in the simulations.

The choice of reference segregating element for the calculations is another factor which needs to be cautiously selected. Strong solute segregation is needed for the interface to be located effectively, and where this was not the case in the $Ba_{0.61}K_{0.39}Fe_2As_2$ datasets, this method was not able to identify the physical extent of the grain boundary. This was also seen in simulations from cases 5 and 6, where the method sometimes failed to identify the interface bounds (see supplementary material). These were scenarios where there was no bin measured with a solute count higher than the calculated threshold; therefore, the code was unable to define the location of the boundary, and so it was not possible to calculate the Gibbsian excess. For case 5, this is due to high solute counts in both the matrix and grain boundary, whilst for case 6, this was caused by the small increase in solute counts at boundaries. This issue was further aggravated by lower spatial resolutions. The findings of the real APT datasets also highlight the importance of carefully choosing the reference segregating element, with Fig. 5(c) showing Gibbsian excess changes depending on which element was used. This is likely due to the differences in field evaporation behaviour of various elements [49], for example using oxygen as the reference resulting in a broader segregation profile than antimony (Fig. 7). Using a different reference element such as Fe can lead to even larger variations in the calculated excess, so it is important that users test a range of reference elements and justify their final choice. Moreover, there can be differences in the order of field evaporation of elements at the interface [50,51], especially in materials like Ba-122, where there are large variations in the evaporation fields of their constitutive elements (e.g. 7 V nm^{-1} for K compared to 42 V nm^{-1} for As) [52]. This can mean the segregation of different elements appears to be at different spatial locations in the reconstructed data (Fig. 10), and could negatively affect the accuracy of the calculated Gibbsian excess. Users should therefore check the order and the distribution of segregating elements for each material studied under APT using this method.

Another key consideration for this method is establishing the size and placement of the region of interest used to extract ion counts across a grain boundary. Because segregation is not always uniform across different regions within the grain boundary plane, and smaller ROIs give larger statistical errors, Gibbsian excess values can vary widely depending on the precise volume and location of the ROI [53–55]. Therefore, ensuring the ROI is placed across as much of the interface as possible will minimise uncertainty in the counts and, in turn, the calculated excess values. Furthermore, to reduce errors, ROIs must be placed with the analysis direction perpendicular to the grain boundary plane, with the limitation that some interfaces are not perfectly planar (which can lead to both broadening of the solute segregation profile [42] and an underestimation of the sampled interface area). The ROI should also include as much of grains A and B as possible, to correctly establish the average grain solute counts and minimise issues caused by noise where bins have higher counts than the set threshold values. Longer ROIs could also improve the accuracy of excess results when grains have different solute concentrations.

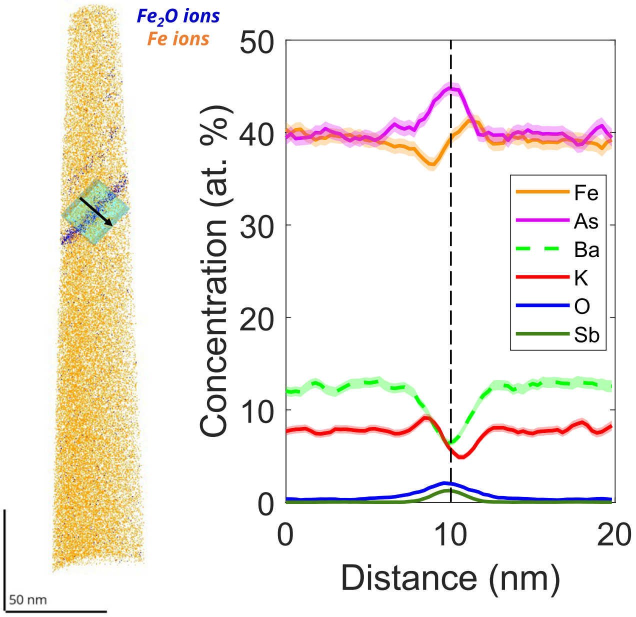

Fig. 10. Concentration profile across a grain boundary of a $Ba_{0.61}K_{0.39}Fe_2As_2$ dataset showing an artificial offset in the segregation profiles of Fe and K compared to that of the other elements in the material. The dashed line represents the estimated location of the grain boundary.

Improvements to this computational method are also possible to maximise the accuracy of Gibbsian excess calculations through higher APT spatial resolutions. This could be achieved by optimising APT analysis conditions, including reducing the analysis temperature, using voltage instead of laser mode, and targeting grain boundaries oriented perpendicularly to the analysis direction (through methods such as Transmission Kikuchi Diffraction (TKD) [56]). Improved spatial resolutions could also open the possibility of extracting accurate grain boundary widths from APT data. In practice, however, this is difficult to accomplish as the analysis conditions mentioned above increase the chance of premature sample fractures during atom probe experiments.

5.2. Validity of the simulations

The simulated datasets have some limitations in supporting the validity of the Gibbsian excess obtained using this method. Unlike in the simulations, the density of atoms in APT data can fluctuate due to local changes in the evaporation field [26] or due to surface ion migration effects during APT experiments when using laser mode [57]. To minimise effects from density changes, solute counts against total counts are typically used when calculating excess values [31]. However, these density fluctuations can lead to different total ion counts in each bin, which can influence the calculation of the Poisson distribution in each grain and, in turn, the calculated thresholds and Gibbsian excess.

The simple cubic cell used in the simulations also does not account for some of the limitations when extracting Gibbsian excess in more complicated cases. For example, in systems with AB crystallographic stacking, the calculated Gibbsian excess will be positive or negative depending on whether an A or B plane constitutes the interface, even when the stacking is assumed to be uniform [38]. This could be the case in the $Ba_{0.61}K_{0.39}Fe_2As_2$ samples, which have an I4/mmm crystal structure with alternating layers of Ba, K and Fe, As, respectively.

Finally, the cases studied here may not represent more complex non-uniform solute segregation scenarios in real APT data. For example, cases where the solute concentration decreases and subsequently increases at a boundary (seen for Fe and K in Fig. 10) could prevent identification of the bounds of the interface, limiting the applicability of this method.

In summary, the simulations in this work have proven the validity of the method used to systematically extract Gibbsian interfacial excess from APT datasets. However, the simulations used are a simplified version of real grain boundary structures in APT, and work to include the effects of field evaporation, retention, and more complex segregation cases would be necessary before this method is applied to systems where these artefacts are particularly prevalent. Therefore, this method is most suitable as a metric of comparison between grain boundaries of the same material, run under consistent atom probe conditions, and where there is clear solute segregation to the boundaries.

5.3. Implications for the superconducting properties of Ba-122

Although this study did not find a clear link between synthesis conditions, Gibbsian excess data, and the measured J_c of the Ba-122 samples, the APT results have revealed significant and non-uniform segregation at grain boundaries that could be affecting the superconducting properties. The segregation behaviour was found to differ even when comparing grain boundaries within a single atom probe reconstruction, with varying segregation levels of impurities (Fig. 6), and different matrix elements being segregated or depleted at different boundaries (Fig. 7). This could in part be explained by the complexity of solute segregation at grain boundaries, which depends on multiple factors, including grain misorientation angles and the types of crystallographic planes that form a boundary [58]. Obtaining crystallographic information on the grain boundary misorientations through correlative TEM or TKD would therefore help understand and compare the segregation behaviour in Ba-122 samples. To make statistically significant comparisons between samples made using different conditions, analysing a larger set of grain boundaries would also be necessary. While TKD would provide invaluable complementary information, the authors of this work found it unfeasible to obtain both a high APT sample yield and clear TKD transmission signals on Ba-122 specimens. This is likely due to the relatively heavy ‘Ba’ atoms, which degrade the TKD signal unless the samples are extremely thin [59], or due to the small grain size of these samples and suboptimal orientation of grain boundaries with respect to the viewing direction, meaning there could be overlapping grains contributing to each pixel [60].

In addition, the measured bulk J_c of these Ba-122 samples (Fig. 9(a)) is affected by multiple competing factors, including the fundamental intragrain properties of the K-doped ‘122’ phase [61,62], the connectivity between ‘122’ grains after the 2nd stage sintering process, and the flux pinning landscape.

Considering the intragrain properties, although no large differences in the average composition of the Ba-122 bulks were found through XRD Rietveld refinement [47], the APT data showed that the Fe to As ratios were not always 1:1 within grains, which could affect the local T_c. However, the overall APT compositions across the three samples were comparable and showed the expected ‘122’ stoichiometry.

Regarding the connectivity at the macroscale, evidence was found in this work of macroscopic cracks present in the bulk samples, which are expected to greatly decrease the magnitude of the measured J_c, as well as larger FeAs and oxide particles seen in EDX (see supplementary material). At the nanoscale, previous work has concluded that the intergrain connectivity is largely compromised by extrinsic factors including porosity [24,63,64], chemical segregation [14,16,65,66], and impurities (typically oxides forming insulating layers [16,67]). We have not observed the secondary FeAs phase wetting layers at grain boundaries reported by some authors [14,18], which must have severe effects on the local current carrying capacity, but the levels of segregation (Fe, As, and K) and impurities (O, Na, and Sb) seen in the rather high purity materials in this study are likely to reduce the intergrain connectivity in these bulk samples to some degree.

However, grain boundaries in Ba-122 could also enhance flux pinning through δT_c pinning. This form of pinning is caused by local reductions in the T_c from the intrinsic distortion of the crystal lattice at grain boundaries, as well as K or Ba segregation or depletion (since the T_c is strongly linked to the doping levels, with the peak in T_c occurring at $x = 0.36$ in $K_xBa_{1-x}Fe_2As_2$) [12,68]. A previous study showed effective grain boundary flux pinning and an inverse relationship between magnetic J_c and grain size in Co-doped Ba-122 [19]. Therefore, the different grain sizes across the three Ba-122 samples in this work (Fig. 9(b)) could have contributed to the variations in the measured J_c (Fig. 9(a)). The density of grain boundaries might also affect how much solute collects at them, but this work did not show any strong correlation between grain size and segregation levels at grain boundaries.

As a result, the overall J_c in ‘122’ bulk samples will depend on a subtle balance between enhancement of J_c through GB pinning and deterioration of $\mathrm{J_c}$ through reduced connectivity at grain boundaries [69]. In this work, the sample with the smallest grain size showed the lowest overall J_c and the largest field dependence, typically associated with poor connectivity and weak-link behaviour. This shows that J_c is likely being dominated by the reduced order parameter at unclean grain boundaries. On the other hand, the sample with the largest grain size (65 MJ kg^{-1}) did not show the highest J_c, but it had a less pronounced field dependence than the finest-grained (200 MJ kg^{-1}) sample. This weaker field-dependence indicates the largest-grained sample likely contained fewer weak-links, and its low J_c at low fields could be the result of its high FeAs phase fraction (Fig. 9(c)). However, FeAs was not found to form wetting layers at the grain boundaries studied with APT (in contrast to what has been seen in previous studies [14,18]), and the FeAs particles seen in the EDX results are too far apart to decrease the macroscopic connectivity very significantly. Therefore, other factors like cracks could have caused the lower J_c seen in the 65 MJ kg^{-1} sample. The highest overall $\mathrm{J_c}$ seen in the 100 MJ kg^{-1} sample may therefore be the result of a larger grain size with fewer weak-linked grain boundaries than the 200 MJ kg^{-1} sample, a lower FeAs fraction than the 65 MJ kg^{-1} sample, and an absence of macroscopic defects like cracks.

This work undoubtedly shows a complex interplay between the many factors that influence J_c behaviour, making it difficult to separate the contributions of individual microstructural features to the superconducting properties. The chemistry variations found in these APT datasets have provided insight into some of these factors that limit J_c in Ba-122 materials. While perfectly clean grain boundaries may provide intrinsic limits to the achievable J_c values [70], there is still clear evidence of significant impurity segregation expected to influence the extrinsic current-carrying capacity of these interfaces, and there is room for improvements in the synthesis protocols to yield cleaner, better-connected grain boundaries. Achieving a J_c closer to the intrinsic limit may therefore be possible through clean synthesis of polycrystalline Ba-122 with small grain sizes.

6. Conclusions

In summary, a computational method to extract Gibbsian interfacial excess across grain boundaries in atom probe datasets has been investigated. The effects of a range of independent variables and composition cases were explored using simulated datasets of known Gibbsian excess. It was found that the accuracy of this method can be high but is limited by cases where there is not enough solute segregation at grain boundaries, and where there are large variations in solute concentration across grains. Careful consideration of the employed bin widths, reference segregating element, ROI placement and size must also be taken.

The method developed and presented in this work provides a systematic way of analysing grain boundaries in Ba-122 materials to confirm how clean they are. In this work, it was applied to calculate and compare the Gibbsian excess in grain boundaries of three $Ba_{0.61}K_{0.39}Fe_2As_2$ samples studied using APT. The results clearly show how complex the grain boundary chemistry in Ba-122 materials is, with inhomogeneous segregation of Fe, As, K, Ba, and impurities of O, Na, and Sb at boundaries. No clear correlation between segregation levels and J_c was found, indicating other factors such as grain size, FeAs phase fractions, porosity, cracks, the upper critical field and T_c could be responsible for the differences in J_c seen across the three samples studied. However, the results in this study highlight the potential for further improving J_c by optimising processing to produce clean grain boundaries.

Declaration of competing interest

The authors declare that they have no known competing financial interests or personal relationships that could have appeared to influence the work reported in this paper.

CRediT authorship contribution statement

Laura Lain Rodriguez: Writing – original draft, Visualization, Software, Methodology, Investigation, Formal analysis, Conceptualization. **Benjamin M. Jenkins:** Writing – original draft, Visualization, Software, Methodology, Investigation, Formal analysis, Conceptualization. **Shah Alam Limon:** Resources, Methodology, Investigation, Formal analysis. **Chiara Tarantini:** Writing – review & editing, Supervision, Methodology, Conceptualization. **Eric Hellstrom:** Writing – review & editing, Supervision, Methodology, Conceptualization. **Fumitake Kametani:** Writing – review & editing, Supervision, Methodology, Conceptualization. **Michael P. Moody:** Writing – review & editing, Supervision, Methodology, Funding acquisition, Conceptualization. **Chris R.M. Grovenor:** Writing – review & editing, Supervision, Methodology, Funding acquisition, Conceptualization. **Susie Speller:** Writing – review & editing, Supervision, Methodology, Funding acquisition, Conceptualization.

Acknowledgements

The atom probe facilities at the University of Oxford are funded by the EPSRC grants EP/M022803/1 and EP/T011505/1. This work was also funded by EPSRC grants EP/W524311/1 and EP/T517811/1, and supported by the US Department of Energy Office of High Energy Physics under the Grant Number DE-SC0018750, the National Science Foundation Cooperative Agreements NSF DMR2128556, and by the State of Florida. The authors acknowledge use of characterisation facilities within the David Cockayne Centre for Electron Microscopy, Department of Materials, University of Oxford, alongside financial support provided by the Henry Royce Institute (Grant ref EP/R010145/1).

BMJ would like to acknowledge funding from the NEUtron iRradiatiOn of advaNced stEels (NEURONE) programme via Fusion Futures. As announced by the UK Government in October 2023, Fusion Futures aims to provide holistic support for the development of the fusion sector. The authors would also like to thank Joshua Winger for his help with collecting X-ray tomography data.

Supplementary materials

Supplementary material associated with this article can be found, in the online version, at doi:10.1016/j.jmst.2026.01.024.

References

[1] H.K. Onnes, Comm. Phys. Lab. Univ. Leiden 122 (1911) 122–124.
[2] D. Larbalestier, A. Gurevich, D.M. Feldmann, A. Polyanskii, Nature 414 (2001) 368–377.
[3] M. Rotter, M. Tegel, D. Johrendt, Phys. Rev. Lett. 101 (2008) 107006.
[4] Y. Kamihara, T. Watanabe, M. Hirano, H. Hosono, J. Am. Chem. Soc. 130 (2008) 3296–3297.
[5] H. Yang, H. Luo, Z. Wang, H.-H. Wen, Appl. Phys. Lett. 93 (2008) 142506.
[6] V. Braccini, A. Xu, J. Jaroszynski, Y. Xin, D.C. Larbalestier, Y. Chen, G. Carota, J. Dackow, I. Kesgin, Y. Yao, A. Guevara, T. Shi, V. Selvamanickam, Supercond. Sci. Technol. 24 (2010) 035001.
[7] B. Sarangi, J.S. Sandra, C.R. Aramadaka, G. Majkic, J. Jaroszynski, V. Selvamanickam, Superconductivity 15 (2025) 100184.
[8] M.M. Altarawneh, K. Collar, C.H. Mielke, N. Ni, S.L. Bud'ko, P.C. Canfield, Phys. Rev. B 78 (2008) 220505.
[9] T. Katase, Y. Ishimaru, A. Tsukamoto, H. Hiramatsu, T. Kamiya, K. Tanabe, H. Hosono, Nat. Commun. 2 (2011) 1–6.
[10] S. Pyon, T. Ito, T. Sasaki, R. Sakagami, T. Tamegai, S. Awaji, H. Kajitani, Physica C 615 (2023) 1354354.
[11] H. Huang, C. Yao, C. Dong, X. Zhang, D. Wang, Z. Cheng, J. Li, S. Awaji, H. Wen, Y. Ma, Supercond. Sci. Technol. 31 (2017) 015017.
[12] S. Ishida, D. Song, H. Ogino, A. Iyo, H. Eisaki, M. Nakajima, J. Shimoyama, M. Eisterer, Phys. Rev. B 95 (2017) 014517.
[13] M. Han, C. Dong, C. Yao, Z. Zhang, Q. Zhang, Y. Gong, H. Huang, D. Gong, D. Wang, X. Zhang, F. Liu, Y. Sun, Z. Zhu, J. Li, J. Luo, S. Awaji, X. Wang, J. Xie, H. Hosono, Y. Ma, Adv. Mater. 37 (2025) e13265.
[14] C. Pak, Y.F. Su, Y. Collantes, C. Tarantini, E.E. Hellstrom, D.C. Larbalestier, F. Kametani, Supercond. Sci. Technol. 33 (2020) 084010.
[15] J.D. Weiss, J. Jiang, A.A. Polyanskii, E.E. Hellstrom, Supercond. Sci. Technol. 26 (2013) 074003.
[16] F. Kametani, Y.-F. Su, Y. Collantes, C. Pak, C. Tarantini, D. Larbalestier, E. Hellstrom, Appl. Phys. Express 13 (2020) 113002.
[17] M. Putti, I. Pallecchi, E. Bellingeri, M.R. Cimberle, M. Tropeano, C. Ferdeghini, A. Palenzona, C. Tarantini, A. Yamamoto, J. Jiang, J. Jaroszynski, F. Kametani, D. Abraimov, A. Polyanskii, J.D. Weiss, E.E. Hellstrom, A. Gurevich, D.C. Larbalestier, R. Jin, B.C. Sales, A.S. Sefat, M.A. McGuire, D. Mandrus, P. Cheng, Y. Jia, H.H. Wen, S. Lee, C.B. Eom, Supercond. Sci. Technol. 23 (2010) 034003.
[18] J.D. Weiss, C. Tarantini, J. Jiang, F. Kametani, A.A. Polyanskii, D.C. Larbalestier, E.E. Hellstrom, Nat. Mater. 11 (2012) 682–685.
[19] Y. Shimada, A. Yamamoto, Y. Hayashi, K. Kishio, J.-I. Shimoyama, S. Hata, T.J. Konno, Supercond. Sci. Technol. 32 (2019) 084003.
[20] H. Hilgenkamp, J. Mannhart, Appl. Phys. Lett. 73 (1998) 265–267.
[21] T.-G. Wang, J.-J. Cao, X.-F. Gou, Appl. Surf. Sci. 480 (2019) 765–769.
[22] H. Salamati, P. Kameli, Solid State Commun. 125 (2003) 407–411.
[23] L.T. Romano, P.R. Wilshaw, N.J. Long, C.R.M. Grovenor, Supercond. Sci. Technol. 1 (1989) 285.
[24] F. Kametani, Y. Su, C. Tarantini, E. Hellstrom, A. Matsumoto, H. Kumakura, K. Togano, H. Huang, Y. Ma, Appl. Phys. Express 17 (2024) 013004.
[25] S. Tokuta, Y. Shimada, A. Yamamoto, Supercond. Sci. Technol. 33 (2020) 094010.
[26] B. Gault, M.P. Moody, J.M. Cairney, S.P. Ringer, Atom Probe Microscopy, Springer, New York, 2012.
[27] Y.-J. Kim, J.D. Weiss, E.E. Hellstrom, D.C. Larbalestier, D.N. Seidman, Appl. Phys. Lett. 105 (2014) 162604.
[28] Z.-H. Sung, A. Masi, J.-Y. Lee, A. Duchenko, X. Bing, D. Isheim, D.N. Seidman, G. Celentano, IEEE Trans. Appl. Supercond. 34 (2024) 1–4.
[29] Z.-H. Sung, A. Masi, J. Lee, A. Duchenko, X. Hu, A.G. Kim, G. Celentano, IOP Conf. Ser. Mater. Sci. Eng. 1302 (2024) 012035.
[30] J.W. Gibbs, The Collected Works of J. Willard Gibbs, Yale Univ. Press, New Haven, 1948.
[31] B.W. Krakauer, D.N. Seidman, Phys. Rev. B 48 (1993) 6724–6727.
[32] B.M. Jenkins, F. Danoix, M. Gouné, P.A. Bagot, Z. Peng, M.P. Moody, B. Gault, Microsc. Microanal. 26 (2020) 247–257.
[33] C. Tarantini, S.A. Limon, K. Mao, E.E. Hellstrom, F. Kametani, Supercond. Sci. Technol. 38 (2025) 045023.
[34] D.J. Larson, D.T. Foord, A.K. Petford-Long, T.C. Anthony, I.M. Rozdilsky, A. Cerezo, G.W.D. Smith, Ultramicroscopy 75 (1998) 147–159.
[35] K. Thompson, B. Gorman, D. Larson, B. van Leer, L. Hong, Microsc. Microanal. 12 (2006) 1736–1737.
[36] C.P. Bean, Rev. Mod. Phys. 36 (1964) 31–39.
[37] E.M. Gyorgy, R.B. van Dover, K.A. Jackson, L.F. Schneemeyer, J.V. Waszczak, Appl. Phys. Lett. 55 (1989) 283–285.
[38] M.W. Finnis, Phys. Status Solidi A 166 (1998) 397–416.
[39] C. Hatzoglou, B. Radiguet, G.D. Costa, P. Pareige, M. Roussel, M. Hernandez-Mayoral, C. Pareige, J. Nucl. Mater. 522 (2019) 64–73.
[40] B.M. Jenkins, A. Zakirov, F. Vurpillot, A. Etienne, C. Pareige, P. Pareige, B. Radiguet, Acta Mater. 281 (2024) 120384.
[41] J. Zelenty, A. Dahl, J. Hyde, G.D.W. Smith, M.P. Moody, Microsc. Microanal. 23 (2017) 269–278.
[42] N. Maruyama, G.D.W. Smith, A. Cerezo, Mater. Sci. Eng. A 353 (2003) 126–132.
[43] D. Blavette, P. Duval, L. Letellier, M. Guttmann, Acta Mater. 44 (1996) 4995–5005.
[44] F. Vurpillot, in: W. Lefebvre-Ulrikson, F. Vurpillot, X. Sauvage (Eds.), Atom Probe Tomography, Academic Press, 2016, pp. 183–249.
[45] M. Morita, M. Karasawa, T. Asaka, M. Owari, J. Surf. Anal. 20 (2014) 177–181.

[46] Z. Šidák, J. Am. Stat. Assoc. 62 (1967) 626–633.
[47] S.A. Limon, Effects of Synthesis Parameters On Superconducting Properties of Polycrystalline K-Doped Ba-122, Florida State University, 2024.
[48] L. Tegg, J.M. Cairney, J. Microsc. 298 (2025) 262–273.
[49] P.J. Felfer, B. Gault, G. Sha, L. Stephenson, S.P. Ringer, J.M. Cairney, Microsc. Microanal. 18 (2012) 359–364.
[50] D.G. Brandon, Surf. Sci. 5 (1966) 137–146.
[51] F. Vurpillot, D. Larson, A. Cerezo, Surf. Interface Anal. 36 (2004) 552–558.
[52] T.T. Tsong, Surf. Sci. 70 (1978) 211–233.
[53] P. Felfer, J. Cairney, Ultramicroscopy 189 (2018) 61–64.
[54] Z. Peng, Y. Lu, C. Hatzoglou, A. Kwiatkowski da Silva, F. Vurpillot, D. Ponge, D. Raabe, B. Gault, Microsc. Microanal. 25 (2019) 389–400.
[55] B. Jenkins, Improving the Safety and Reliability of Reactor Pressure Vessel Steels, ProQuest Dissertations & Theses, 2019.
[56] K. Babinsky, R. De Kloe, H. Clemens, S. Primig, Ultramicroscopy 144 (2014) 9–18.
[57] A. Cerezo, G.D.W. Smith, P.H. Clifton, Appl. Phys. Lett. 88 (2006) 154103.
[58] M. Herbig, D. Raabe, Y.J. Li, P. Choi, S. Zaefferer, S. Goto, Phys. Rev. Lett. 112 (2014) 126103.
[59] R.R. Keller, R.H. Geiss, J. Microsc. 245 (2012) 245–251.
[60] S. Suzuki, JOM 65 (2013) 1254–1263.
[61] F. Kurth, K. Iida, S. Trommler, J. Hänisch, K. Nenkov, J. Engelmann, S. Oswald, J. Werner, L. Schultz, B. Holzapfel, S. Haindl, Supercond. Sci. Technol. 26 (2013) 025014.
[62] J. Engelmann, K. Iida, F. Kurth, C. Behler, S. Oswald, R. Hühne, B. Holzapfel, L. Schultz, S. Haindl, Physica C 494 (2013) 185–188.
[63] Z. Gao, K. Togano, A. Matsumoto, H. Kumakura, Sci. Rep. 4 (2015) 4065.
[64] L. Wang, Y. Qi, D. Wang, X. Zhang, Z. Gao, Z. Zhang, Y. Ma, S. Awaji, G. Nishijima, K. Watanabe, Physica C 470 (2010) 183–186.
[65] F. Kametani, P. Li, D. Abraimov, A.A. Polyanskii, A. Yamamoto, J. Jiang, E.E. Hellstrom, A. Gurevich, D.C. Larbalestier, Z.A. Ren, J. Yang, X.L. Dong, W. Lu, Z.X. Zhao, Appl. Phys. Lett. 95 (2009) 142502.
[66] Q.-P. Ding, T. Prombood, Y. Tsuchiya, Y. Nakajima, T. Tamegai, Supercond. Sci. Technol. 25 (2012) 035019.
[67] L. Wang, Y. Ma, Q. Wang, K. Li, X. Zhang, Y. Qi, Z. Gao, X. Zhang, D. Wang, C. Yao, C. Wang, Appl. Phys. Lett. 98 (2011) 222504.
[68] S. Avci, O. Chmaissem, D.Y. Chung, S. Rosenkranz, E.A. Goremychkin, J.P. Castellan, I.S. Todorov, J.A. Schlueter, H. Claus, A. Daoud-Aladine, D.D. Khalyavin, M.G. Kanatzidis, R. Osborn, Phys. Rev. B 85 (2012) 184507.
[69] K. Iida, J. Hänisch, A. Yamamoto, Supercond. Sci. Technol. 33 (2020) 043001.
[70] J.H. Durrell, C.-B. Eom, A. Gurevich, E.E. Hellstrom, C. Tarantini, A. Yamamoto, D.C. Larbalestier, Rep. Prog. Phys. 74 (2011) 124511.